August 10, 2021

The Deep Ocean's Carbon Exhaust

Haidi Chen[1], F. Alexander Haumann[1*], Lynne D. Talley[3], Kenneth S. Johnson[4], and Jorge L. Sarmiento[1]

[1]Atmospheric and Oceanic Sciences Program, Princeton University, Princeton, NJ, USA.

[3]Scripps Institution of Oceanography, University of California, San Diego, La Jolla, California, USA.

[3]Monterey Bay Aquarium Research Institute, Moss Landing, California, USA.

*Corresponding author: F. Alexander Haumann (alexander.haumann@gmail.com)

Key Points:

- Deep ocean CO_2 release arises from high potential CO_2 partial pressure in subsurface water between the Subantarctic Front and sea-ice edge
- Maximum subsurface potential CO_2 conincides with the outcrop of upwelling Indo-Pacific Deep Water, rich in remineralized organic carbon
- High alkalinity and low temperature prevent CO_2 release from high carbon-content deep water outcropping south of Indo-Pacific Deep Water

Abstract

The deep ocean naturally releases large amounts of old, pre-industrial carbon dioxide (CO_2) to the atmosphere through upwelling in the Southern Ocean, closing the global ocean carbon cycle. This Southern Ocean CO_2 release is relevant to the global climate, because its changes could alter atmospheric CO_2 levels on long time scales and the present-day potential of the Southern Ocean to take up anthropogenic CO_2. Here, based on observational data, we show that this CO_2 release arises from a zonal band of subsurface waters between the Subantarctic Front and wintertime sea-ice edge with a potential partial pressure of CO_2 exceeding current atmospheric CO_2 levels (ΔPCO_2) by 175 µatm. This band of high ΔPCO_2 subsurface water conincides with the outcropping of the 27.8 kg m^{-3} isoneutral density surface that marks the upwelling of Indo-Pacific Deep Water (IPDW). Vertically, the IPDW layer exhibits a distinct ΔPCO_2 maximum in the deep ocean, which is set by remineralization of organic carbon and originates from the northern Pacific and Indian Ocean basins. Below this IPDW layer, the carbon content increases downwards, whereas ΔPCO_2 decreases. Most of this vertical ΔPCO_2 decline results from decreasing temperatures and increasing alkalinity due to an increased fraction of calcium carbonate dissolution. These two factors limit the CO_2 outgassing from the high-carbon content deep waters on more southerly surface outcrops. Our results imply that the response of Southern Ocean CO_2 fluxes to possible future changes in upwelling are sensitive to the subsurface carbon chemistry set by the vertical remineralization and dissolution profiles.

1 Introduction

Based on year-round biogeochemical measurements with profiling floats, recent work has identified a larger than previously estimated release of carbon dioxide (CO_2) from the Southern Ocean to the atmosphere during austral winter (black line in Figure 1; Bushinsky et al., 2019; Gray et al., 2018). While there has been a broad consensus that the region south of about 50°S releases old, pre-industrial CO_2 to the atmosphere (Gruber et al., 2019; Mikaloff Fletcher et al., 2007; Morrison et al., 2015; Wu et al., 2019), the magnitude and extent of this CO_2 release have been substantially smaller in previous estimates, which were derived from ship-board measurements (gray and red lines in Figure 1; Landschützer et al., 2016, 2020; Takahashi et al., 2009). These smaller previous estimates largely arise from a lack of data during austral winter, when deep mixing stirs waters with elevated partial pressure of CO_2 (pCO_2) to the surface. In this study, we analyze observations from ships and floats measured at depth that are not prone to large seasonal variations in order to address the question if such a large outgassing from the Southern Ocean during winter can be expected when deep waters are brought to the surface. We aim to further our understanding of the underlying mechanisms of this deep ocean CO_2 release in the Southern Ocean and to identify its sources.

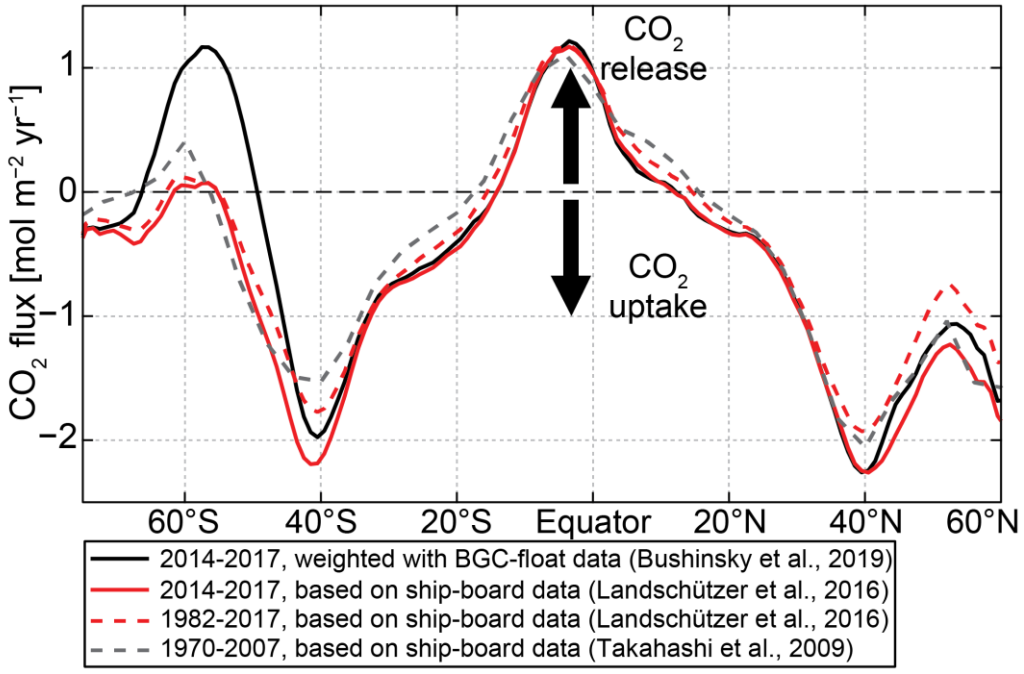

Figure 1. Zonal and annual mean global ocean to atmosphere CO_2 flux (positive values denote ocean CO_2 release to the atmosphere) from different data products for different time periods.

Black: Neural-network estimate, weigthed with biogeochemical Argo float data (Bushinsky et al., 2019; Landschützer et al., 2019). Red: Neural-network estimate, based on ship-board observations from the SOCAT database (Landschützer et al., 2016, 2020). Gray: Climatology based on ship-board observations from the CDIAC database (Takahashi et al., 2009).

In the Southern Ocean (south of about 50°S), CO_2 is naturally released from the ocean to the atmosphere due to the upwelling of carbon-rich waters from the deep layers of the global ocean (Mikaloff Fletcher et al., 2007; Morrison et al., 2015; Takahashi et al., 2009; Wu et al., 2019). Globally, the Southern Ocean CO_2 release is balanced by CO_2 uptake in the subtropics and northern subpolar oceans (Figure 1; Gruber et al., 2009; Takahashi et al., 2002, 2009). This CO_2 uptake is driven in part by cooling of the surface water as it is being transported to higher latitudes, which increases its capacitiy to hold CO_2, and in part by the sinking of biologically produced organic matter out of the surface layer (Gruber et al., 2009; Takahashi et al., 2002, 2009). The biologically produced organic carbon sinks through the thermocline and is being remineralized at depth, where it feeds the deep waters with inorganic carbon, which is then transported to the Southern Ocean (Sarmiento & Gruber, 2006). Therefore, the upwelling and CO_2 release in the Southern Ocean closes the global ocean carbon cycle.

The leakage of old, pre-industrial CO_2 from the deepest ocean layers is unique to the high-latitude Southern Ocean, because this is the only region where deep waters ascend to the surface along rising, steep isopycnals (Morrison et al., 2015; Speer et al., 2000; Talley, 2013; Toggweiler & Samuels, 1995). Deep waters exit the Indian, Pacific and Atlantic basins in both western and eastern boundary currents, and spiral southeastward and upward until reaching the base of the mixed layer in the southern Antarctic Circumpolar Current (ACC; Tamsitt et al., 2017, 2019). This upwelling process is thought to be the major return pathway for remineralized carbon from the ocean's interior to the surface (Kwon et al., 2009; Sarmiento et al., 1988; Skinner et al., 2010). Estimates of ocean transport show that a supply of dissolved inorganic carbon (DIC) to the Southern Ocean surface comes from a southward and upward flux of Circumpolar Deep Water (CDW; Iudicone et al., 2011; Wu et al., 2019). This southward transport consists of North Atlantic Deep Water (NADW), Lower Circumpolar Deep Water (LCDW) in the Indian and Pacifc basins, and somewhat less dense Indo-Pacific Deep Water (IPDW) that all carry DIC from sinking and remineralization of biogenic carbon, and, in the case of NADW, DIC from air-sea gas exchange (Aldama-Campino et al., 2020; Broecker & Peng, 1992).

In this study, we seek to explain the characteristic meridional patterns of surface CO_2 fluxes in the Southern Ocean (Figure 1), to explain why CO_2 release peaks in a zonal band between 55°S and 60°S, and to identify the pathway and sources of how the deep ocean loses carbon to the atmosphere. For this purpose, we assess factors that could affect the deep ocean's outgassing potential using subsurface DIC, alkalinity, and nutrient data from ship-based observations (Key et al., 2004, 2015; Lauvset et al., 2016; Olsen et al., 2016) and biogeochemical floats (Johnson et al., 2017). In order to relate these ocean observational data to the Southern Ocean surface CO_2 fluxes, in a first step, we here make use of the interior ocean potential pCO_2 (PCO_2; Broecker & Peng, 1982; Skinner et al., 2010) excess above the approximate current (year 2015) global-mean atmospheric pCO_2 (pCO_2^{atm} = 400 µatm), i.e. $\Delta PCO_2 = PCO_2 - pCO_2^{atm}$. Thus, we calculate the seawater PCO_2 as the pCO_2 that a water parcel would attain if it were adiabatically brought to the surface (Broecker & Peng, 1982) using its DIC, alkalinity, potential temperature (θ) and sea-level pressure. The resulting ΔPCO_2 is then a more accurate measure of the capability of upwelling water to release CO_2 to the present-day atmosphere than DIC alone. In a second step, we analyze the drivers of the spatial patterns of ΔPCO_2 in the interior ocean by estimating the different contributions of the dissolution, solubility, gas exchange and biological carbon pump processes (Gruber & Sarmiento, 2002; Sarmiento & Gruber, 2006; Volk & Hoffert, 1985). In a third step, we decompose ΔPCO_2 vertical gradient into components associated with DIC, temperature, and alkalinity. Using this decomposition, we demonstrate the importance of considering the full vertical carbon chemistry structure, in particular alkalinity, when assessing the influence of the carbon-rich deep ocean on the surface Southern Ocean CO_2 fluxes.

2 Methods

2.1 Potential *p*CO2 and neutral density

Potential pCO_2 (PCO_2) is defined as the pCO_2 that a water parcel would attain if it was brought to the surface adiabatically (Broecker & Peng, 1982; Sarmiento & Gruber, 2006; Skinner et al., 2010), thus correcting for the pressure effects on temperature and partial pressure. PCO_2 is computed following Williams et al. (2017) using CO2SYS (van Heuven et al., 2011) and by using dissociation constants of carbonate from Lueker et al. (2000), of sulfate from Dickson (1990), and of fluoride from Perez & Fraga (1987), and the boron to salinity ratio of Lee et al. (2010). Here,

PCO_2 is a function of alkalinity (Alk), DIC, potential temperature (θ, referenced to 0 dbar), practical salinity (S), the reference pressure (p^{ref} = 0 dbar), silicate (Si), and phosphate (PO_4). For biogeochemical float data (section 3), we use nitrate (NO_3) and convert it to PO_4 and Si using stoichiometric phosphate-to-nitrate and silicate-to-nitrate ratios of 1:16 and 2.5, respectively (Anderson & Sarmiento, 1994). Note that we here use the deviation of the interior ocean PCO_2 from the approximate current (year 2015) atmospheric pCO_2 of 400 μatm (ΔPCO_2) to illustrate the present-day outgassing potential of an interior ocean water mass, which differs from past or future atmospheric conditions.

We here evaluate the interior ocean ΔPCO_2 structure considering neutral density surfaces. For this purpose, we have calculated the neutral density (γ^n) for all data sets (section 3) based on Jackett & McDougall (1997; version 3.05.12; 17th June, 2019; http://www.teos-10.org/preteos10_software/neutral_density.html). Since in this code γ^n is not defined for temperatures below −2.5 °C, any possible temperature below this value is set to −2.5 °C.

2.2 Dilution and solubility

In a first step, we estimate the effect of dilution of ocean tracers through freshwater fluxes on PCO_2 (ΔPCO_2^{dil}) by evaluating the difference between PCO_2 and $sPCO_2$ derived from salinity normalized (s) quantities:

$$\Delta PCO_2^{dil} = PCO_2 - sPCO_2. \quad (1)$$

Here, $sPCO_2$ is derived using sAlk, sDIC, sSi, and sPO_4, whereas salinity normalization of a given variable X to a reference salinity (S^{ref} = 34.7) is performed through (Broecker & Peng, 1992; Chen & Millero, 1979)

$$sX = \frac{X}{S} S^{ref}. \quad (2)$$

The only exception here is sDIC, which we obtain by first salinity normalizing its preindustrial value and then adding the anthropogenic component (see section 3).

In a second step, we estimate the effect of solubility on the interior ocean PCO_2 distribution (ΔPCO_2^{sol}) through

$$\Delta PCO_2^{sol} = sPCO_2 - PCO_2^{DIC,Alk}. \quad (3)$$

Here, $PCO_2^{DIC,Alk}$ is the PCO_2 arising from variations in sDIC and sAlk and it is computed as a function of sAlk, sDIC, θ^{ref} (2.5 °C), S^{ref} (34.7), p^{ref} (0 dbar), sSi, and sPO_4. Reference values θ^{ref} and S^{ref} are arbitrary values that depend on the purpose of the analysis. The resulting ΔPCO_2^{sol} provides a measure for the contribution of mostly temperature differences relative to the location of the reference value. Since we are interested in the ocean interior structure of PCO_2, we chose these reference values to reflect deep water properties. If e.g. θ^{ref} was set to 20 °C, which is closer to global surface water temperatures, the interior ocean $PCO_2^{DIC,Alk}$ would become much larger than the actual PCO2 and ΔPCO_2^{sol} strongly negative everywhere.

2.3 Biological pumps

We further attribute the interior ocean ΔPCO_2 variations to the driving biological pump components, i.e. the soft-tissue and carbonate pumps that are associated with the photosynthesis and remineralization of organic matter as well as the precipitation and dissolution of calcium carbonate ($CaCO_3$), respectively. We make use of a concept that has been developed to separate the interior ocean DIC variations into these contributions (Gruber & Sarmiento, 2002; Sarmiento & Gruber, 2006; Volk & Hoffert, 1985) to estimate their effect on ΔPCO_2. In order to achieve this goal, we first separately estimate the sDIC, sAlk, sPO_4 and sSi deviations from their global-mean surface reference values, which are listed in Table 1, defined as $\Delta X = sX - sX^{ref}$, for any variable X. For $sDIC^{ref}$, we use the estimated pre-industrial surface mean value, since the effect of anthropogenic carbon is estimated separately (sections 2.4 and 3). Since the surface ocean sPO_4, is most likely also affected by anthropogenic activity, we chose a sPO_4^{ref} that is lower than the global mean surface value. We lower sPO_4^{ref} so that a small positive residual ΔPCO_2 residual in the deep northern Pacific becomes zero. We expect this region to have a zero residual ΔPCO_2 because the effects of air-sea gas exchange, which are reflected by the residual (section 2.4), should be neglible in the deep northern Pacific where waters have been isolated from the atmosphere for thousands of years (Holzer et al., 2021). We note that sPO_4^{ref} value chosen here is also close to the value used by Gruber & Sarmiento (2002).

Table 1. Reference values used in this study for the estimation of the drivers of interior ocean PCO_2 variations, in part derived from gridded GLODAPv2 data (Lauvset et al., 2016).

Variable	Value	Description
p^{ref}	0 dbar	Reference pressure

S^{ref}	34.7	Reference ocean salinity
θ^{ref}	2.5 °C	Reference ocean temperature
pCO_2^{atm}	400 µatm	Approximate atmospheric partial pressure of CO_2 in 2015
PCO_2^{ref}	131 µatm	Partial pressure of CO_2 using reference values of this table
$sAlk^{ref}$	2298 µmol kg^{-1}	Reference surface ocean alkalinity
sPO_4^{ref}	0.1 µmol kg^{-1}	Reference surface ocean phosphate concentration
sSi^{ref}	6.3 µmol kg^{-1}	Reference surface ocean silicate concentration
$sDIC^{ref}$	1967 µmol kg^{-1}	Reference preindustrial surface ocean dissolved inorganic carbon concentration

The contributions of the soft-tissue pump to the ΔDIC and ΔAlk are then estimated as

$$\Delta DIC^{soft} = r_{C:P}\,\Delta PO_4, \tag{4}$$

and

$$\Delta Alk^{soft} = -\,r_{C:N}\,\Delta DIC^{soft}, \tag{5}$$

respectively. Here, $r_{C:P}$ and $r_{N:C}$ are the carbon-to-phosphate and nitrate-to-carbon stoichiometric ratios set to 117/1 and 16/117, respectively (Anderson & Sarmiento, 1994). The latter ratio is applied because a molar increase in seawater nitrate due to e.g. the remineralization of organic matter equals the molar decline in Alk (Sarmiento & Gruber, 2006).

Subsequently, the contributions of the carbonate pump to the ΔDIC and ΔAlk are estimated as

$$\Delta Alk^{carb} = \Delta Alk - \Delta Alk^{soft}, \tag{6}$$

and

$$\Delta DIC^{carb} = 0.5\,\Delta Alk^{carb}, \tag{7}$$

respectively.

In contrast to DIC and Alk, PCO_2 is not a conserved tracer but depends on current carbon chemistry and solubility of the water. Therefore, separating ΔPCO_2 deviations into its components is not straightforward. Nevertheless, we can quantify the range of values by calculating each contribution, i.e. ΔPCO_2^{soft} and ΔPCO_2^{carb}, under four scenarios, during which we vary processes that modify the PCO_2 sensitivity to DIC and Alk, and using p^{ref}, S^{ref}, and θ^{ref}.

The first scenario for ΔPCO_2^{soft} assumes that the soft-tissue pump is the only process influencing DIC and Alk deviations from the reference values. As such, ΔPCO_2^{soft} is calculated by using sDIC, sAlk, sPO_4, and sSi fields that are driven by the soft-tissue pump alone:

$$\Delta PCO_2^{soft} = PCO_2(sDIC^{ref} + \Delta DIC^{soft}, sAlk^{ref} + \Delta Alk^{soft}, sPO_4, sSi) - PCO_2^{ref}. \quad (8)$$

where PCO_2^{ref} is the ocean PCO_2 calculated using all reference values (Table 1). The second and third scenarios assume that one of the two other processes influencing DIC and Alk, i.e. carbonate pump and gas exchange (section 2.4), has occurred prior to the soft-tissue pump to determine the PCO_2 sensitivity to DIC and Alk. Therefore, we quantify ΔPCO_2^{soft} as the PCO_2 difference between when both the soft-tissue pump and carbonate pump are operating and that when only the carbonate pump is active:

$$\Delta PCO_2^{soft} = PCO_2(sDIC^{ref} + \Delta DIC^{carb} + \Delta DIC^{soft}, sAlk^{ref} + \Delta Alk^{carb} + \Delta Alk^{soft}, sPO_4, sSi) - PCO_2\left(sDIC^{ref} + \Delta DIC^{carb}, sAlk^{ref} + \Delta Alk^{carb}, sPO_4^{ref}, sSi^{ref}\right), \quad (9)$$

and as the PCO_2 difference between when both the soft-tissue pump and gas exchange (including the anthropogenic component) are operating and that when only gas exchange is active:

$$\Delta PCO_2^{soft} = PCO_2(sDIC^{ref} + \Delta DIC^{gasex} + \Delta DIC^{cant} + \Delta DIC^{soft}, sAlk^{ref} + \Delta Alk^{soft}, sPO_4, sSi) - PCO_2\left(sDIC^{ref} + \Delta DIC^{gasex} + \Delta DIC^{cant}, sAlk^{ref}, sPO_4^{ref}, sSi^{ref}\right). \quad (10)$$

where ΔDIC^{gasex} and ΔDIC^{cant} are defined in sections 2.4 and 3, respectively. The last scenario is that ΔPCO_2^{soft} occurs after all the other processes to change the PCO_2 sensitivity. Therefore, we have

$$\Delta PCO_2^{soft} = PCO_2(sDIC, sAlk, sPO_4, sSi) - PCO_2\left(sDIC - \Delta DIC^{soft}, sAlk - \Delta Alk^{soft}, sPO_4^{ref}, sSi^{ref}\right). \quad (11)$$

We then use the mean of the four scenarios (equations 8 to 11) as an estimate for the contribution of the ΔPCO_2^{soft} to the interior ocean ΔPCO_2 distribution. ΔPCO_2^{carb} is estimated following the same procedure.

2.4 Air-sea gas exchange

We proceed to estimate the effect of air-sea gas exchange on the interior ocean ΔPCO_2 distribution. For this purpose, we separately consider the pre-industrial gas exchange (ΔDIC^{gasex}) and its anthropogenic component, by using ΔDIC^{cant} estimates (Lauvset et al., 2016; see section 3) and calculating ΔDIC^{gasex} as the residual of all other terms:

$$\Delta DIC^{gasex} = sDIC - sDIC^{ref} - \Delta DIC^{cant} - \Delta DIC^{soft} - \Delta DIC^{carb}. \quad (12)$$

We then apply the same approach as outlined in equations 8 to 11, but replacing the soft-tissue pump components with the respective gas exchange components, yielding estimates for ΔPCO_2^{gasex} and ΔPCO_2^{cant}.

2.5 Impact of carbon chemistry and solubility on the vertical ΔPCO_2 distribution

To quantify how the water carbon chemistry and solubility effects drive the vertical ΔPCO_2 distribution, we separately estimate the departure of ΔPCO_2 due to deviations of DIC, Alk, and θ and S, from the respective reference values (Table 1). The increasing DIC with depth is the primary source of the elevated ΔPCO_2 in the deeper layers of the ocean, which is then modified by Alk, θ, and S. Therefore, we first estimate PCO_2 variations due to DIC alone (ΔPCO_2^{DIC}):

$$\Delta PCO_2^{DIC} = PCO_2^{DIC} - PCO_2^{ref} = PCO_2(sDIC, sAlk^{ref}, \theta^{ref}, S^{ref}, sPO_4, sSi) - PCO_2^{ref}. \quad (13)$$

We then estimate the impact of Alk variations (ΔPCO_2^{Alk}) as

$$\Delta PCO_2^{Alk} = PCO_2^{DIC,Alk} - PCO_2^{DIC} - PCO_2^{ref} \quad (14)$$

where, $PCO_2^{DIC,Alk}$ is defined in section 2.2. Moreover, we define $\Delta PCO_2^{DIC,Alk} = PCO_2^{DIC,Alk} - pCO_2^{atm}$.

3 Data

Our conclusions are drawn from ship-based measurements and measurements by profiling floats. We use physical and biogeochemical data from the gridded Global Ocean Data Analysis Project version 2 (GLODAPv2; Key et al., 2004, 2015; Lauvset et al., 2016; Olsen et al., 2016) climatology, which are provided at a 1° by 1° spatial resolution. GLODAPv2 is based on shipboard measurements from 724 hydrographic cruises from 1972 to 2013. Estimates of anthropogenic DIC

239 provided in the mapped GLODAPv2 data (Lauvset et al., 2016) were used to assess the
240 anthropogenic contribution to DIC. The GLODAPv2 DIC and ΔDIC^{cant} estimates are referenced
241 to the year 2002. In addition, we use biogeochemical profiling float data from a broad region in
242 the Southern Ocean (Johnson et al., 2021), which were deployed as part of the Southern Ocean
243 Carbon and Climate Observations and Modeling (SOCCOM) project (Johnson et al., 2017). Here,
244 we use a total of 8332 profiles from 174 floats with measurements of high-quality pH (Johnson et
245 al., 2016; Williams et al., 2017), NO_3, and estimated Alk (Carter et al., 2018) to estimate PCO_2.

246 Surface CO_2 flux data stems from two neural-network estimates; one is weighted towards
247 biogeochemical Argo float data (Bushinsky et al., 2019; Landschützer et al., 2019) and one uses
248 only shipboard observations from the SOCAT database (Landschützer et al., 2016, 2020). A third
249 product is a climatology based on shipboard observations from the CDIAC database (Takahashi
250 et al., 2009). Climatological frontal positions stem from Orsi et al. (1995) and the sea-ice edge
251 position is the annual mean 1% sea-ice concentration from the merged product distributed through
252 the Climate Data Record (1979 to 2018; Meier et al., 2017; Peng et al., 2013).

253 **4 Results**

254 **4.1 Spatial patterns of CO_2 release linked to subsurface ΔPCO_2 maximum**

255 The float-weighted annual mean surface CO_2 flux estimate (Bushinsky et al., 2019; Landschützer
256 et al., 2019) reveals a distinct ring feature (Figure 2a,b), with strong CO_2 release occurring within
257 the ACC, roughly between the Subantarctic Front and the winter-time sea-ice edge. The highest
258 outgassing occurs in the Pacific and Indian Ocean sectors, regionally exceeding 3 mol m^{-2} yr^{-1}
259 (positive values are a CO_2 flux from the ocean to the atmosphere; see also Prend et al., submitted).
260 In these regions, intensive CO_2 release is observed in the fall and winter, followed by weaker, yet
261 non-negligible, outgassing fluxes in the remaining seasons (Bushinsky et al., 2019; Gray et al.,
262 2018). North of the ACC, CO_2 fluxes are characterized by a broad region of CO_2 uptake. The
263 highest annual uptake, below −3 mol m^{-2} yr^{-1}, is found in the Argentine Basin in the Atlantic,
264 characterized by a strong uptake mostly occurring between spring to fall. In the seasonally ice-
265 covered region, annual mean surface CO_2 fluxes are generally small. In summary, the largest CO_2
266 release occurs roughly between the sea-ice edge and the Subantarctic Front during wintertime, a

region that is dominated by a wind-driven divergence at the surface and deep mixing in winter (Bushinsky et al., 2019; Gray et al., 2018; Prend et al., submitted).

The ring pattern of outgassing evident from the surface CO_2 fluxes aligns with the region of upward sloping isopycnal surfaces in the Southern Ocean subsurface between about 50°S and 65°S (Figure 2c,d). In this region, the zonal mean ΔPCO_2 from the float profiles reveals a signature of high-ΔPCO_2 deep water that upwells along isopycnals. The vertical ΔPCO_2 maximum appears along the 27.8 kg m^{-3} neutral density surface, which shoals towards the south within the ACC; this is coincident with the core of the oxygen minimum layer that is characteristic of, and defines, IPDW (Talley, 2013; see also Figure 3g-i). The sign of the surface CO_2 fluxes (Figure 2b) closely tracks this the shoaling of the subsurface ΔPCO_2 maximum (Figure 2c), switching from CO_2 uptake north of 50°S to CO_2 outgassing between about 50°S and 65°S (Figure 2b). Maximum outgassing, between 55°S and 60°S, encompasses the latitude range of positive ΔPCO_2 at the surface (gray contour lines in Figure 2c). This picture of highest surface outgassing in the region where high-ΔPCO_2 waters upwell, as derived from the profiling floats, is corroborated by a ring pattern in the ΔPCO_2 constructed from gridded shipboard observations (section 3) at 800 m depth (Figure 2e). It reflects the high annual-mean surface CO_2 fluxes, with highest values occurring between the Polar and Subantarctic Front. The core of the subsurface high-ΔPCO_2 ring coincides with the outcropping of the 27.8 kg m^{-3} neutral density surface (black in Figure 2c,e). Both the surface CO_2 fluxes and the subsurface ΔPCO_2 at 800 m decrease further south of the outcropping 27.8 kg m^{-3} neutral density surface. Therefore, the reduced CO_2 outgassing south of its maximum is in part related to a decrease of the subsurface ΔPCO_2 south of 60°S. In addition, the inhibition of gas exchange by sea-ice cover, a potentially high biological carbon export efficiency (Arteaga et al., 2018), reduced mixing (Wilson et al., 2019), and cold surface temperatures could further limit the mixed-layer ΔPCO_2 and thereby surface CO_2 fluxes in this seasonally ice-covered region. In summary, the outcropping of the isopycnal surfaces in the Southern Ocean acts to project the vertical ΔPCO_2 structure with its maximum on the 27.8 kg m^{-3} neutral density surface onto a horizontal plane, resulting in the meridional ΔPCO_2 maximum between the sea-ice edge and Subantarctic Front.

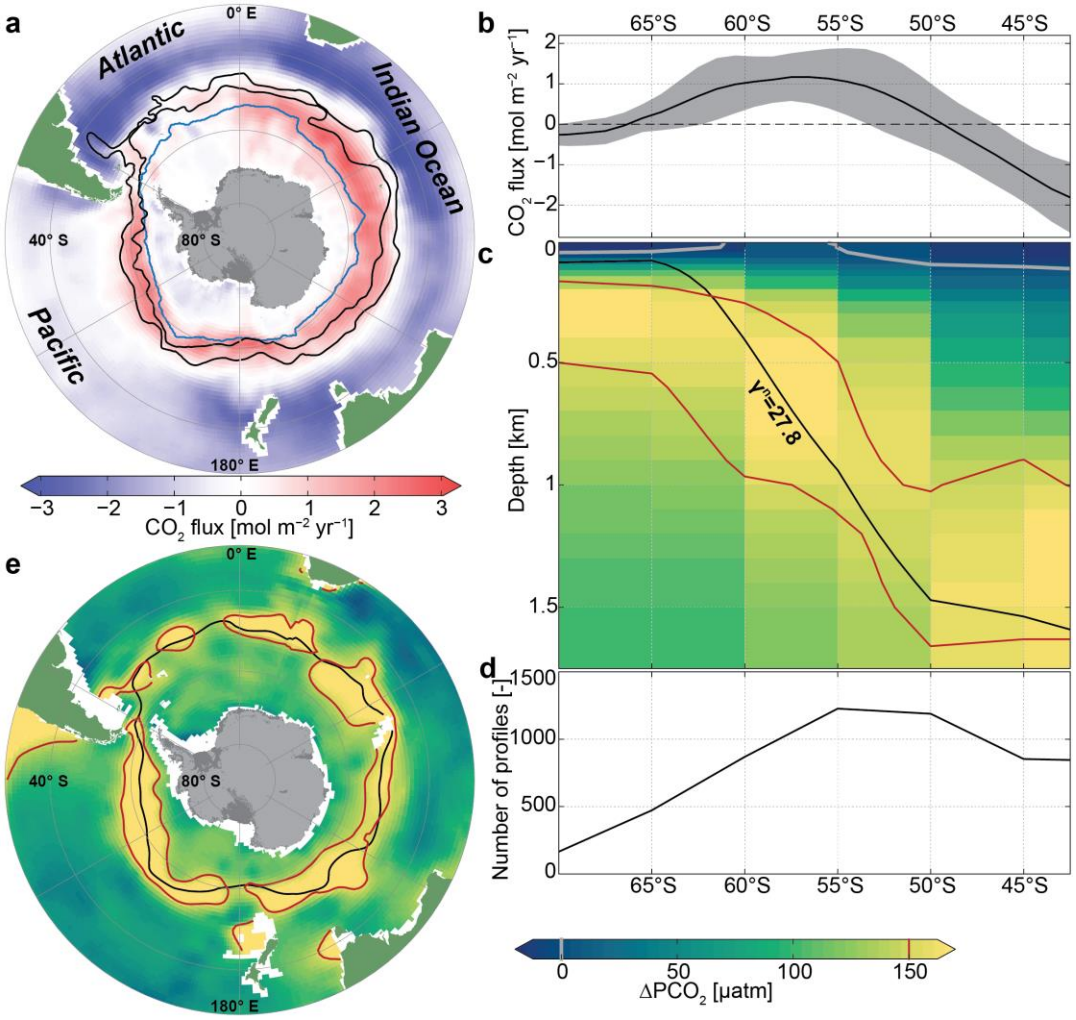

Figure 2. Southern Ocean CO_2 release and its subsurface source. **a,** Annual mean surface CO_2 flux from a neural-network estimate that is weighted with biogeochemical Argo float data (Bushinsky et al., 2019; Landschützer et al., 2019). Positive values (red) indicate CO_2 degassing from the ocean to the atmosphere. Black contours denote the mean position of the Subantarctic and Polar Fronts (Orsi et al., 1995). The light blue contour line represents the annual mean sea-ice edge (1% mean sea-ice concentration). **b,** Zonally averaged annual mean surface CO_2 flux (as in panel a). Gray shading denotes ±1 standard deviation in the zonal direction. **c**, Zonally averaged annual-mean potential pCO_2 excess with respect to current atmospheric levels (400 µatm; ΔPCO_2) from profiling floats (in 5° latitudinal bins). **d**, Number of float profiles per 5° latitudinal bins. **e**, ΔPCO_2 at 800 m from gridded GLODAPv2. In **c** and **e**, the 27.8 kg m^{-3} isoneutral surface is shown in black, and the 150 µatm and 0 µatm ΔPCO_2 isolines in red and gray, respectively.

4.2 Sources of the subsurface ΔPCO_2 maximum

Where does the high subsurface ΔPCO_2 water in the Southern Ocean come from? In order to address this question, in the following, we base our anlaysis ΔPCO_2 derived from a global data set

(GLODAPv2; Lauvset et al., 2016; see section 3) as displayed in Figure 3. Note that this data has several advantages, such as higher accuracy ship-board observations compared to the float data, actual alkalinity observations, and being a gridded product. However, major difference occur at the Southern Ocean surface. Here, the float data suggest an outcrop of the zero ΔPCO_2 contour (gray in Figure 2c), whereas the the zero ΔPCO_2 contour from ship-data (white in Figure 3a-c) does not outcrop. This difference most likely occurs from the lag of wintertime observations in GLODAPv2. In this study we are mostly interested in the subsurface ΔPCO_2, where both data sets largely agree.

We now assume that, to a first order, water masses spread along isoneutral density surfaces (denoted as γ^N)—an assumption that has been widely used to identify the deep water circulation pathways (Jackett & McDougall, 1997). The ΔPCO_2 maximum follows the 27.8 kg m^{-3} isoneutral surface, which characterizes the IPDW core as identified by the vertical oxygen minimum (Talley, 2013; Figure 3); hence the vertical oxygen and ΔPCO_2 extrema appear to have the same biological and physical forcing. The ΔPCO_2 maximum can be traced back from the Southern Ocean subsurface to its source region in the deep northern Indian and Pacific basins (Figure 3a-c). Here, the ocean is pervaded by PCO_2-rich waters, with ΔPCO_2 much larger than 150 µatm extending from the thermocline to about 4 km depth (red contour line in Figure 3b,c).

The highest ΔPCO_2 waters, indicated by a ΔPCO_2 larger than 800 µatm, are located in the North Pacific between 50ºN and 60ºN and between 500 m and 1500 m, where the oldest subsurface waters occur in the global ocean, supplied by slow vertical diffusion from below (dashed white lines in Figure 3c; Holzer et al., 2021; Talley, 2013). These waters with high ΔPCO_2 spread southward and outcrop at the sea surface in the Southern Ocean (Gent & McWilliams, 1990; Holzer et al., 2021; Talley, 2013). They enter the Southern Ocean as a layer of elevated ΔPCO_2 that extends southward and upward across 50° S, where the zonal mean PCO_2 exceeds atmospheric levels by about 175 µatm (averaged between 27.7 kg m^{-3} and 27.9 kg m^{-3}; Table 2). Both advective and diffusive eddy transport can play an important role in pulling these high ΔPCO_2 signals to the Southern Ocean subsurface (Dufour et al., 2015; Tamsitt et al., 2017), with the final step being entrainment into the surface mixed layer (Prend et al., submitted). This chimney of elevated ΔPCO_2 is narrowly constrained along the IPDW core (27.8 kg m^{-3} isoneutral surface; Figure 3c). As these waters reach the Southern Ocean, the ΔPCO_2 signal is strongly attenuated as a result of diapycnal

mixing with ambient low ΔPCO_2 waters, yet its magnitude is still strongly elevated and forms a clear local vertical maximum. South of the Polar Front, where the 27.8 kg m^{-3} isoneutral surface outcrops, the high ΔPCO_2 signals originated from the IPDW are circumpolarly distributed, again mirroring the oxygen minimum layer (Figure 3g-i; Talley, 2013), and control the subsurface ΔPCO_2 around Antarctica.

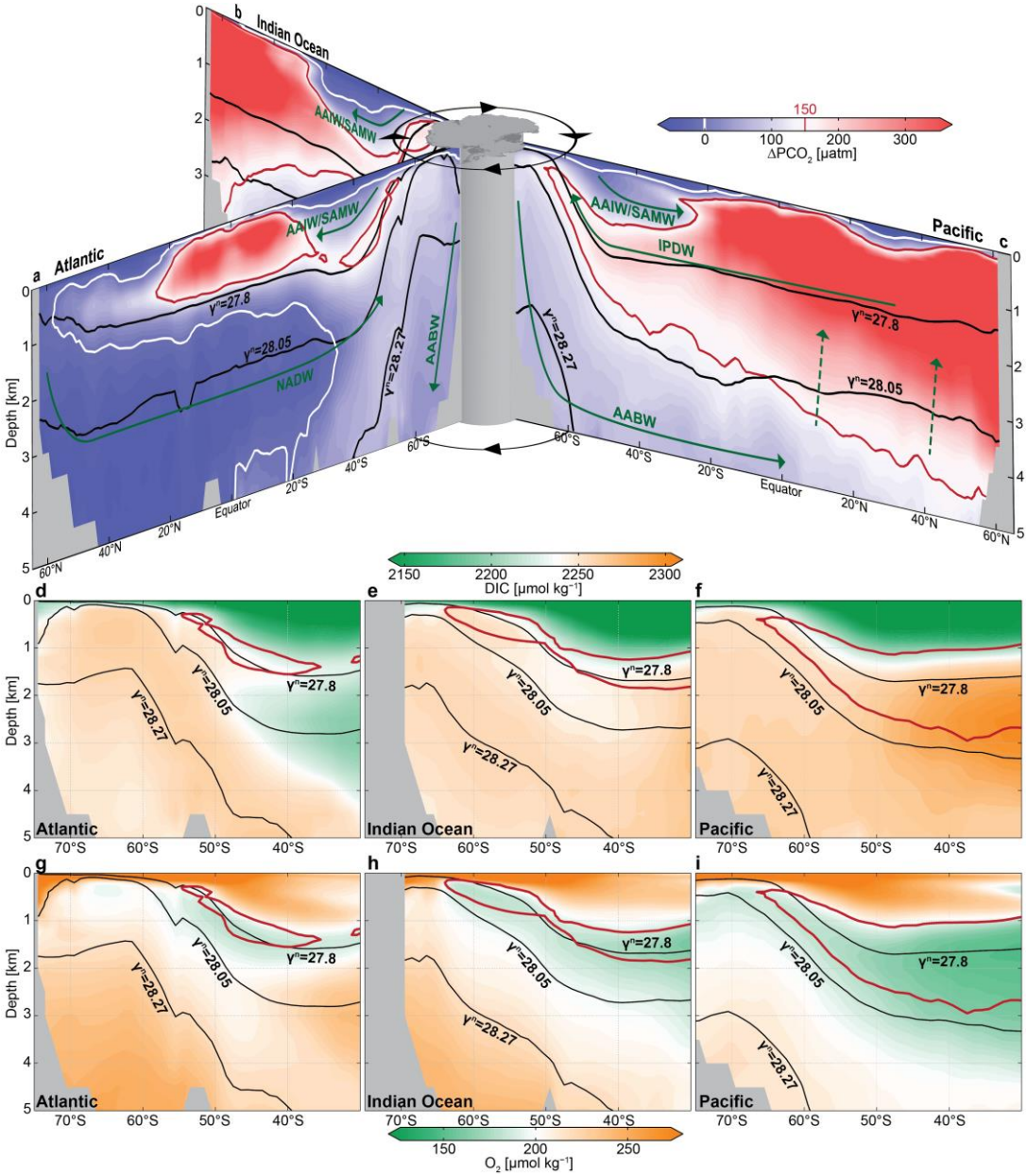

Figure 3. Potential pCO_2 excess above current atmospheric levels (400 µatm; ΔPCO_2) and DIC in the ocean interior from gridded GLODAPv2. Meridional sections of zonally averaged ΔPCO_2 in the Atlantic **(a)**, Indian Ocean **(b)**, and Pacific **(c),** overlaid with a schematic representation of the subsurface water pathways (white arrows) and the ACC (black arrows). Zonally averaged DIC in the Atlantic **(d)**, Indian **(e)**, and Pacific **(f)** sectors of the Southern Ocean (south of 30°S). Zonally

averaged dissolved oxygen (O_2) in the Atlantic **(g)**, Indian Ocean **(h)**, and Pacific **(i)** sectors of the Southern Ocean (south of 30°S). Isoneutral surfaces are shown in black (γ^N = 27.8 and 28.05 kg m^{-3} characterizing IPDW and NADW, respectively), and the 150 µatm and 0 µatm ΔPCO_2 isolines in red and white, respectively.

In contrast to the maximum ΔPCO_2 found in IPDW, the lowest value of deep-ocean ΔPCO_2, of less than −50 µatm, is located in the northern Atlantic, where NADW is formed from surface sources, and hence has higher oxygen and lower ΔPCO_2 than IPDW (Figure 3a,g). The NADW core in the Southern Ocean has been identified by its salinity maximum, which roughly follows the 28.05 kg m^{-3} isoneutral surface (Talley, 2013). While the ΔPCO_2 of NADW increases continuously due to diapycnal mixing and biological processes as the NADW moves southward, much less CO_2 outgassing would be expected if NADW were the primary water mass being ventilated in the Southern Ocean. In the Southern Ocean, NADW mixes with higher ΔPCO_2 LCDW from the Indo-Pacific (Figure 3c). Between 45°S and 55°S, the circumpolar average of LCDW/NADW has a ΔPCO_2 that is about 70 µatm lower than the ΔPCO_2 of IPDW (Table 2). This LCDW/NADW mixture then upwells primarily in the region covered by the seasonal sea ice (Talley, 2013), where the local environment further hinders the air-sea CO_2 exchange. In conclusion, our analysis shows that the characteristic pattern of a high ΔPCO_2 ring below the mixed layer, which causes the Southern Ocean CO_2 outgassing, is induced by the southward and upward transport of IPDW through a narrow and relatively light isoneutral density band and cannot be explained by the upwelling of LCDW, such as NADW.

4.3 Drivers of high ΔPCO_2 in Indo-Pacific Deep Water

Why is ΔPCO_2 particularly elevated along the circulation pathway of IPDW? A larger CO_2 outgassing potential in deep waters has generally been linked to a higher DIC content. However, IPDW has no clear DIC maximum in the Southern Ocean (Figure 3d-f). Instead, vertically, the DIC peaks are located at a much greater depth and higher density than those of ΔPCO_2. For example, DIC maxima in the Southern Ocean occur on isoneutral surfaces that are associated with the Antarctic Bottom Water (AABW; $\gamma^N \sim 28.27$ kg m^{-3}; Orsi et al., 1999) in the Atlantic and Indian Ocean (Figure 3d,e), and on isoneutral density surfaces of about 28.0 kg m^{-3} in the Pacific north of 50ºS (Figure 3f). Since the IPDW ΔPCO_2 maximum cannot simply be explained by its carbon content (DIC), we here consider the different physical (dilution, solubility, air-sea gas

exchange; section 4.3.1) and biological processes (soft tissue and carbonate pumps; section 4.3.2), as well as the carbonate chemistry (DIC, Alk; section 4.3.3) that determine the interior Southern Ocean PCO_2 structure (see section 2 for methods). For this purpose, we evaluate these contributions on depth levels (Figures 4, 5, and 6a,b) and on neutral density surfaces that represent the corresponding water masses (Figure 6c,d and Table 2). We vertically separate the subsurface ocean into three neutral density layers: IPDW (27.7 kg m^{-3} – 27.9 kg m^{-3}), LCDW/NADW (27.9 kg m^{-3} – 28.2 kg m^{-3}), AABW (> 28.2 kg m^{-3}; Figure 6 and Table 2).

4.3.1 Physical drivers of interior ocean ΔPCO_2 structure

Physical effects on ΔPCO_2 include the dilution of ocean tracers by surface freshwater fluxes, changes in CO_2 solubility due to variations in the interior ocean temperature and salinity structure, and air-sea gas exchange (section 2.2). Dilution effects (ΔPCO_2^{dil}; Figure 4a-c, Table 2) are generally small (< 5 µatm). Compared to our chosen reference salinity of 34.7, the LCDW/NADW layer (γ^N ~ 28.05 kg m^{-3}) and the subtropical surface waters have an elevated ΔPCO_2^{dil} due to evaporation effects on those waters. Antarctic surface waters, Antarctic Intermediate Water (AAIW), and Subantarctic Mode Water (SAMW) experience a reduced ΔPCO_2^{dil} due to a net freshwater input at the Southern Ocean surface. However, this pattern cannot explain the overall interior ocean ΔPCO_2 structure and its magnitude is negligible.

Solubility effects (ΔPCO_2^{sol}; Figure 4d-f), which are mostly associated with the interior Southern Ocean temperature distribution and to a lesser degree with the salinity distribution, are on the order of about 20 to 100 µatm. They become very large in the much warmer subtropical thermocline waters. Overall, the colder temperatures in the deepest layers, in particular AABW, as well as the high-latitude Antarctic surface waters, reduce ΔPCO_2 and enhance the ability of these waters to hold CO_2 or reduce their outgassing potential. Thus, solubility effects have a substantial influence on the interior Southern Ocean ΔPCO_2 structure and act to contribute to the observed vertical ΔPCO_2 decline, especially in the deepest layers (Figure 6a,b; Table 2). However, vertical ΔPCO_2^{sol} gradients around the ΔPCO_2 maximum (27.8 kg m^{-3}) are weaker than in the abyssal ocean, suggesting that other processes control the ΔPCO_2 decrease with depth, especially between the IPDW and LCDW/NADW layers.

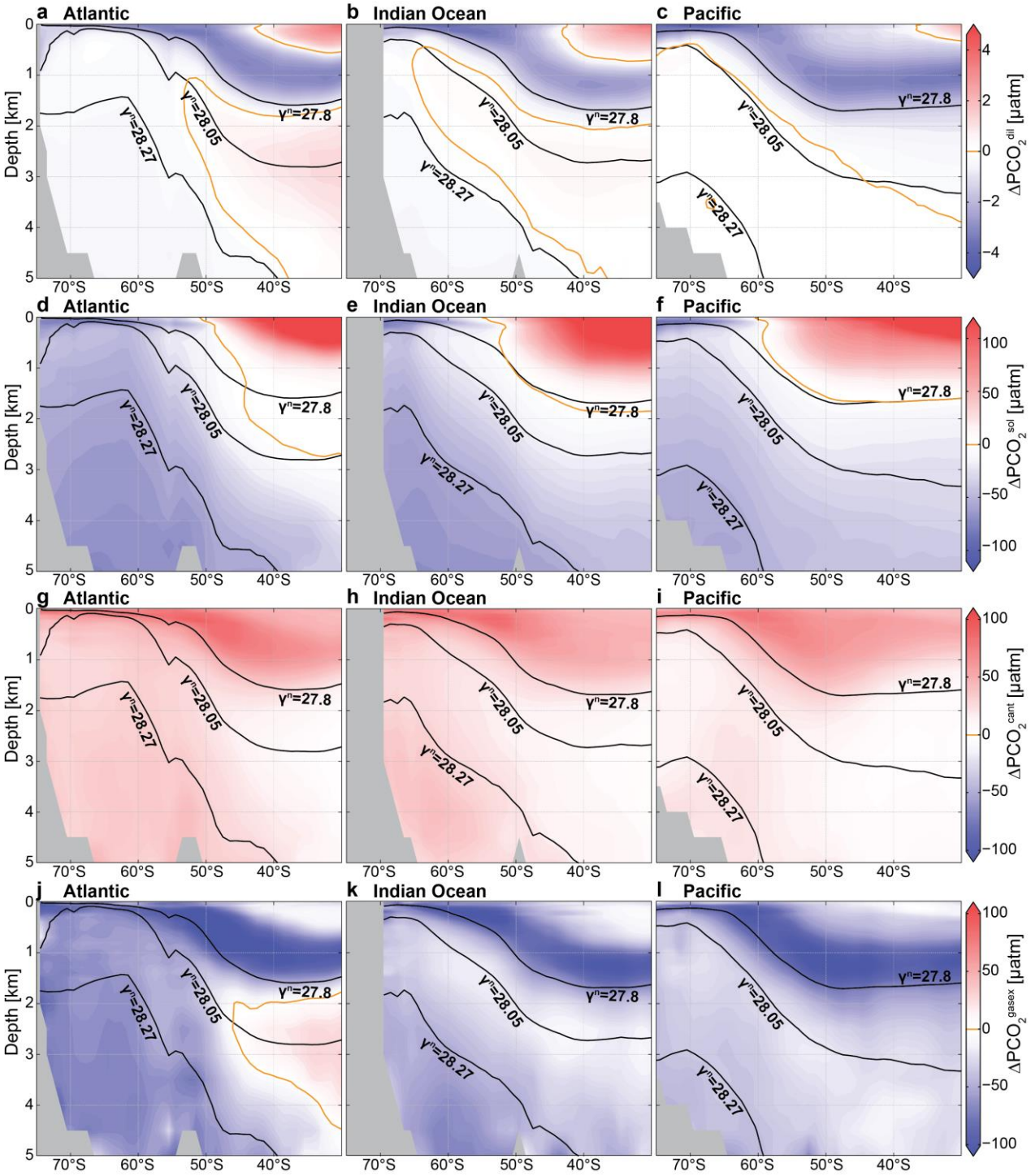

Figure 4. Physical drivers of the subsurface ΔPCO_2 structure. **a–c**, Dilution effects (ΔPCO_2^{dil}) relative to a salinity of 34.7. **d–f,** Solubility effects (ΔPCO_2^{sol}) with respect to a reference temperature and salinity of 2.5 °C and 34.7, respectively. **g–i**, Influence of anthropogenic carbon uptake (ΔPCO_2^{cant}). **j–l**, Influence of air-sea gas exchange (ΔPCO_2^{gasex}). Panels show the Atlantic

(left), Indian (middle), and Pacific (right) sectors of the Southern Ocean. Isoneutral surfaces are shown in black, and the 0 µatm ΔPCO_2 isoline in orange.

For the effect of CO_2 air-sea gas exchange on ΔPCO_2, we split it into its anthropogenic (ΔPCO_2^{cant}; Figure 4g-i) and natural (ΔPCO_2^{gasex}; Figure 4j-l) components, where ΔPCO_2^{cant} is based on the estimate of the anthropogenic carbon content as provided by GLODAPv2 (section 2.4). ΔPCO_2^{cant} is elevated in the AAIW, SAMW, and subtropical surface waters and also has some smaller positive values in the AABW (Gruber et al., 2019). However, a substantial amount of ΔPCO_2^{cant} is also found in IPDW, and the decline of ΔPCO_2^{cant} with depth contributes to the overall vertical ΔPCO_2 decline below IPDW (Table 2). Such an invasion of ΔPCO_2^{cant} to the IPDW layer could arise from along-isopycnal stirring by mesoscale eddies, connecting the surface outcrop of the isopycnal with the older, upwelling deep waters (Abernathey & Ferreira, 2015). ΔPCO_2^{gasex} is largely negative, except in the NADW core (Figure 4j-l). These negative values reflect CO_2 outgassing when waters are at the surface (Gruber et al., 2009). The most negative values of ΔPCO_2^{gasex} are associated with AAIW. This water was formed by transforming the upwelling IPDW into lighter waters at the Southern Ocean surface, mostly through freshening by sea ice and precipitation (Haumann et al., 2016). While it was at the surface it has experienced a substantial loss of CO_2 to the atmosphere (Figure 2a) before the water was subducted as AAIW. Similarly to its anthropogenic component, natural gas exchange effects also reach into the IPDW layer ($\gamma^N \sim$ 27.8 kg m^{-3}). The negative peak of ΔPCO_2^{gasex} just above the 27.8 kg m^{-3} isoneutral surface contributes to the sharp decline of ΔPCO_2 just above the IPDW layer, but counteracts the decline below this layer (Figure 6, Table 2). In summary, solubility effects and anthropogenic carbon enforce, and gas-exchange counteracts the IPDW ΔPCO_2 maximum (Table 2).

4.3.2 Biological drivers of interior ocean ΔPCO_2 structure

In order to better understand the biological contribution to the subsurface ΔPCO_2 structure in the Southern Ocean, we compare the soft-tissue (ΔPCO_2^{soft}) and carbonate (ΔPCO_2^{carb}) pump contributions to ΔPCO_2 variations arising from variations in sDIC and sAlk alone ($\Delta PCO_2^{DIC,Alk}$; Figure 5a-c), i.e. for fixed reference values of temperature, salinity, and pressure (section 2). Note that $\Delta PCO_2^{DIC,Alk}$ equals the sum of PCO_2^{ref}, ΔPCO_2^{soft}, ΔPCO_2^{carb}, ΔPCO_2^{gasex}, and ΔPCO_2^{cant} minus pCO_2^{atm} (section 2). The soft-tissue pump (ΔPCO_2^{soft}) is the most efficient mechanism to increase the deep ocean's ΔPCO_2 through the accumulation of remineralized carbon (DIC; Figure

6 and Table 2). The contribution of this mechanism to ΔPCO_2 explains most of the interior ocean structure of $\Delta PCO_2^{DIC,Alk}$ (Figure 5a-f), as well as the occurrence of very high $\Delta PCO_2^{DIC,Alk}$ in IPDW. High values of ΔPCO_2^{soft} in the rather shallow IPDW (595 µatm; Table 2), as compared to the deeper LCDW/NADW (506 µatm; Table 2), partially occur because IPDW accumulates respired carbon over much longer timescales than the relatively younger NADW (DeVries & Primeau, 2011), which is related to the long route that newly-ventilated AABW takes through the Indian and Pacific, upwelling diffusively to produce IPDW, which then returns to the Southern Ocean surface (Holzer et al., 2021; Talley, 2013). In addition to the difference in accumulation time, IPDW receives more organic carbon from remineralization as a result of its rather shallow depth in the water column (shallower than 1500 m) compared to LCDW/NADW and AABW (Kwon et al., 2009; Martin et al., 1987). The organic matter received by IPDW could be about twice as large as in the layers below when using a vertical organic carbon remineralization curve that follows a classic power-law relationship (Martin et al., 1987) and ignoring possible spatial differences in the production of organic matter at the surface. A secondary peak in both $\Delta PCO_2^{DIC,Alk}$ and ΔPCO_2^{soft} occurs around the 28.27 kg m^{-3} isoneutral surface, which marks the upper bound of AABW (Orsi et al., 1999), in particular in the Weddell Sea (Atlantic south of 50°S; Figure 5a,d). This secondary $\Delta PCO_2^{DIC,Alk}$ peak arises from local production and remineralization within the Weddell Gyre (MacGilchrist et al., 2019). In conclusion, ΔPCO_2^{soft} dominates the vertical ΔPCO_2 decline below IPDW, which also explains the collocation between the vertical ΔPCO_2 maximum and the dissolved oxygen minimum in the deep ocean (section 4.2), because also both quatinties are dominated by the soft-tissue pump.

The magnitude of ΔPCO_2^{soft} (Figure 5d-f) is substantially larger than $\Delta PCO_2^{DIC,Alk}$ (Figure 5a-c), because the carbonate pump (ΔPCO_2^{carb}; Figure 5g-i) counters the soft-tissue pump effect on $\Delta PCO_2^{DIC,Alk}$. This negative ΔPCO_2^{carb} in the deep ocean arises from the dissolution of mineral carbonates, which increases alkalinity twice as much as it increases DIC. The most negative values of ΔPCO_2^{carb} are located in the deep Pacific (Figure 5i), where dissolution of mineral carbonate is enhanced by the metabolic CO_2 release that drives the deep water to be undersaturated with respect to calcite (Broecker & Peng, 1987; Jiang et al., 2015; Kwon et al., 2011; Sarmiento et al., 1988). As the dissolution process strongly depends on pressure and preferentially happens at greater depth compared to organic matter remineralization (Broecker & Peng, 1987; Kwon et al., 2011;

Sarmiento et al., 1988), the ΔPCO_2^{carb} deficit appears to peak at greater depth then the ΔPCO_2^{soft} maximum in the Pacific (Figure 5i). However, due to compensatory effects between the Atlantic and the Pacific basins (Figure 5g,i), the ΔPCO_2^{carb} contribution to the overall zonal mean vertical ΔPCO_2 decline with depth is small (Figure 6a; between 45°S and 55°S) and even of opposite sign when averaged over neutral density layers (Table 2). Therefore, the overall effects of ΔPCO_2^{carb} in setting the vertical ΔPCO_2 maximum in IPDW are small, but are critical to understand the differences between the vertical ΔPCO_2 and DIC profiles, as we show in the following section.

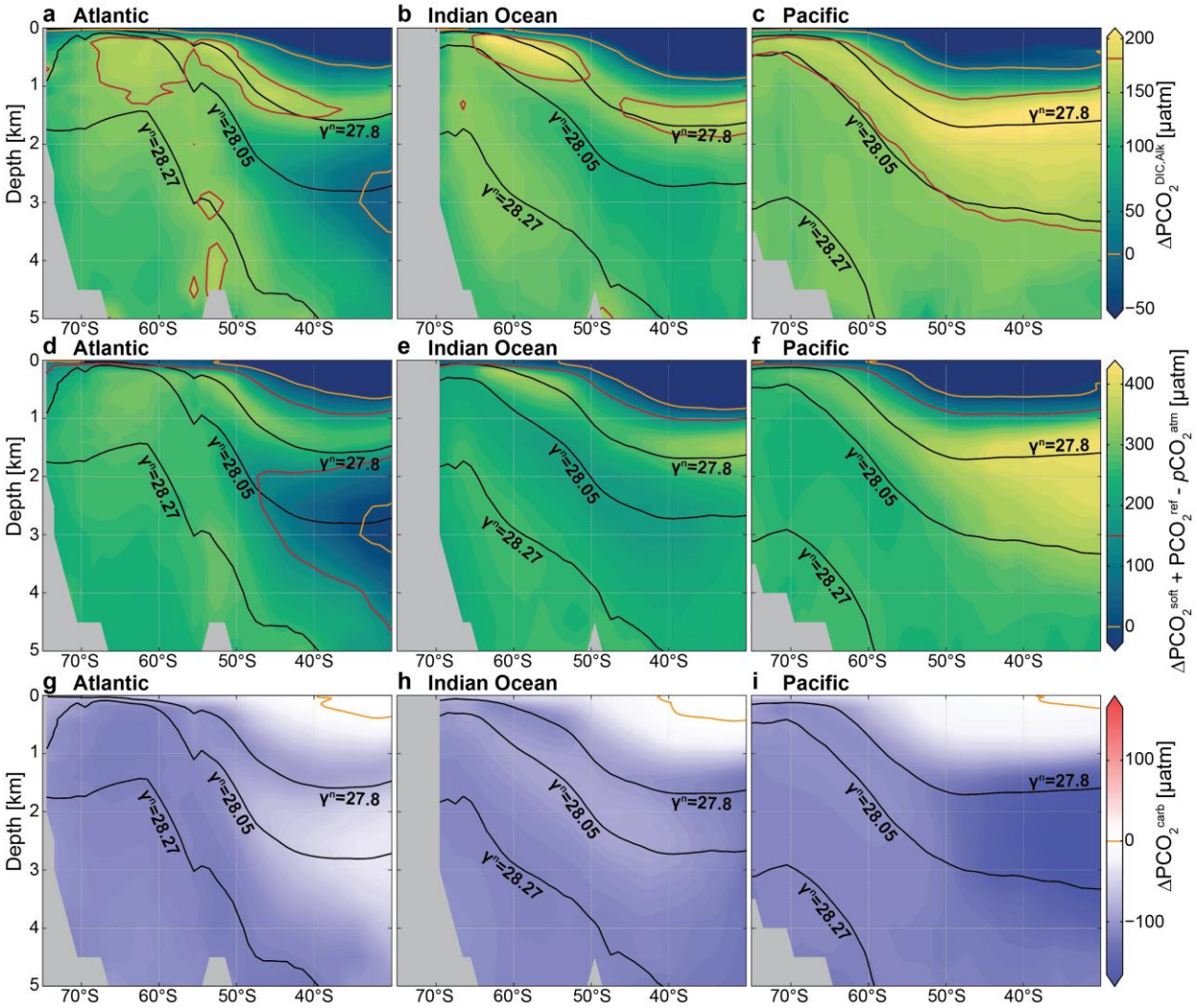

Figure 5. Biological drivers of the subsurface ΔPCO_2 structure. **a–c**, ΔPCO_2 structure due to interior ocean DIC and Alk variations alone ($\Delta PCO_2^{DIC,Alk}$), after removing dilution and solubility effects. **d–f**, Expected ΔPCO_2 driven by the soft-tissue pump (ΔPCO_2^{soft}) due to photosynthesis and remineralization of organic matter plus PCO_2^{ref} (131.5 µatm) minus pCO_2^{atm} (400 µatm). **g–i,** Carbonate pump (ΔPCO_2^{carb}) due to precipitation and dissolution of calcium carbonate. Panels show the Atlantic (left), Indian (middle), and Pacific (right) sectors of the Southern Ocean.

Isoneutral surfaces are shown in black, and the 150 µatm and 0 µatm ΔPCO_2 isolines in red and orange, respectively.

4.3.3 Vertical difference between DIC and ΔPCO_2 maxima between 45°S and 55°S

We now separately consider the effects of DIC and alkalinity on the vertical ΔPCO_2 structure (Figure 6c,d) to better understand why ΔPCO_2 decreases below the 27.8 kg m^{-3} isoneutral surface despite an equally high or higher carbon content (DIC) below this layer in the Southern Ocean (Figure 3). While the soft-tissue and carbonate pumps both act to enhance the DIC storage in the interior ocean, the carbonate pump adds DIC to a greater depth than the soft-tissue pump (Broecker & Peng, 1987; Kwon et al., 2011; Sarmiento et al., 1988). The difference between the vertical ΔPCO_2 and DIC structure then largely results from the vertical alkalinity structure, since the soft-tissue pump decreases the deep ocean alkalinity (increasing ΔPCO_2) and the carbonate pump increases it (decreasing ΔPCO_2). This impact of alkalinity on the zonal mean vertical ΔPCO_2 structure between 45°S and 55°S is shown in Figure 6c,d (see section 2.5). Compared to the ΔPCO_2 maximum of 175 µatm in IPDW, ΔPCO_2 in LCDW/NADW waters is 70 µatm lower (Table 2). The largest contributor to this reduction, i.e. 30 µatm, is alkalinity, while the remainder is explained by a colder temperature and lower DIC (Table 2; Figure 6d). The DIC contribution arises from low-DIC NADW, which vanishes in depth coordinates, where Alk and temperature effects are the sole drivers of the vertical ΔPCO_2 decline with depth (Figure 6c). These roles of alkalinity and temperature in driving a vertical ΔPCO_2 decline become even larger when comparing the IPDW layer to AABW. Thus, the vertical DIC gradient cannot explain the lower ΔPCO_2 in deeper and heavier waters, except for the NADW core ($\gamma^N \sim 28.05$ kg m^{-3}), where it contributes. In conclusion, the separation between the deeper DIC and shallower ΔPCO_2 maxima is caused by the shallower depth of remineralization of organic carbon compared to the depth of dissolution of calcium carbonate that sets the relative contributions of DIC and Alk in driving ΔPCO_2, corroborated by a decreasing temperature with depth.

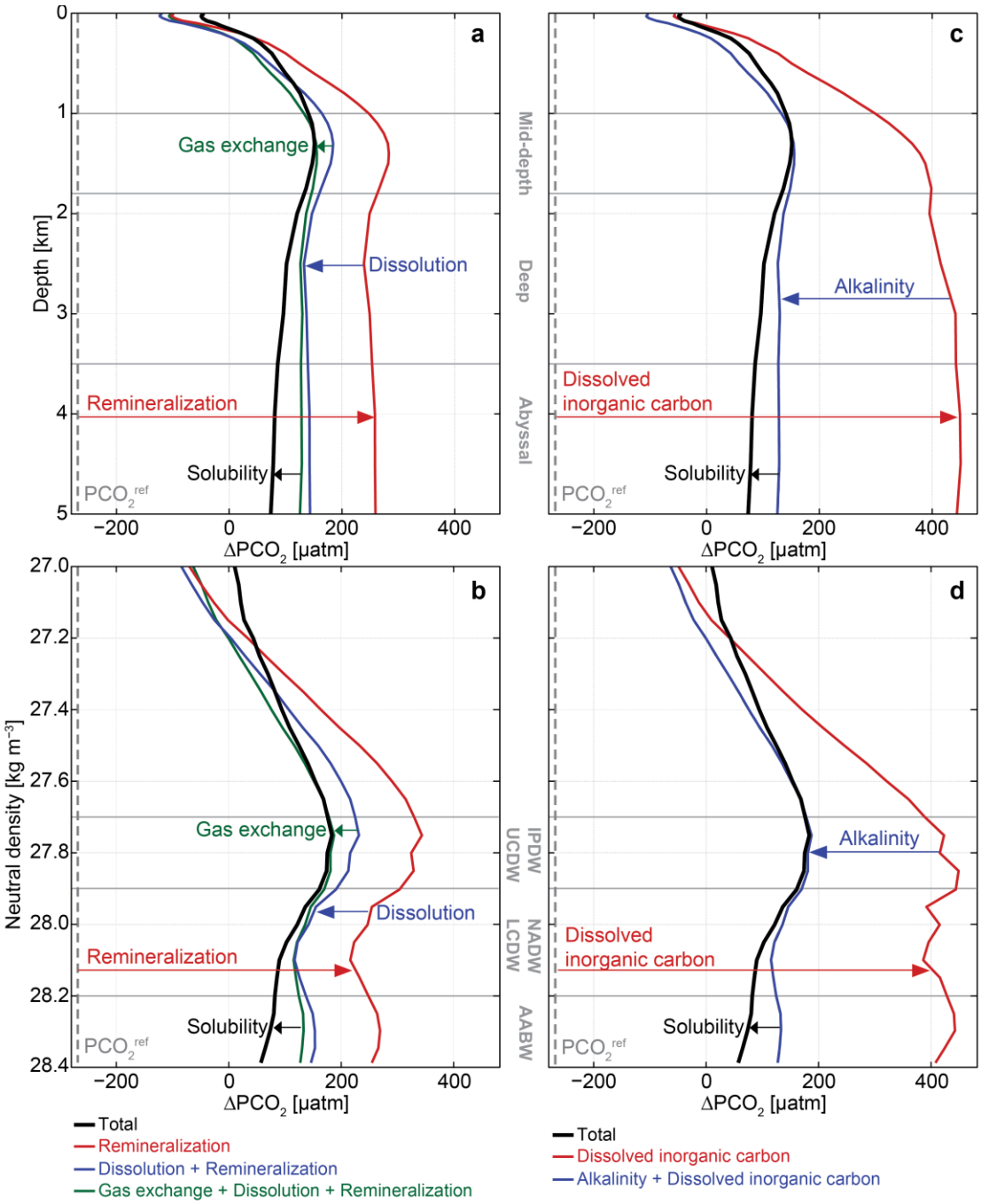

Figure 6. Drivers of the vertical ΔPCO_2 profile between 45°S and 55°S. Decomposition of ΔPCO_2 profiles into biological and physical processes in **(a)** depth and **(b)** neutral density coordinates. Decomposition of ΔPCO_2 profiles into chemical (DIC, Alk) and physical components in **(c)** depth and **(d)** neutral density coordinates. Note that in this figure, for simplicity, gas exchange is the combination of anthropogenic and natural components and dilution effects are neglected.

519 **Table 2.** Deep ocean ΔPCO_2 (in µatm) and its estimated sources averaged for different water
520 masses (columns 2, 3, 4) and differences between water masses and IPDW (columns 5, 6).

Layer	**IPDW**	**LCDW/NADW**	**AABW**	**LCDW/NADW – IPDW**	**AABW – IPDW**
Range	**27.7 kg m^{-3} – 27.9 kg m^{-3}**	**27.9 kg m^{-3} – 28.2 kg m^{-3}**	**> 28.2 kg m^{-3}**		
Total	175	104	77	-70	-97
Dilution	-1	0	0	2	1
Solubility	-4	-23	-53	-19	-48
Remineralization	595	506	530	-89	-65
Dissolution	-112	-104	-114	8	-2
Anthropogenic	39	18	25	-21	-13
Gas exchange	-78	-25	-46	53	33
DIC	657	634	665	-23	8
Alkalinity	-249	-279	-307	-30	-58

521 **5 Conclusions and discussion**

522 We here show that the upwelling of high-ΔPCO_2 IPDW occurs along the 27.8 kg m^{-3} isoneutral
523 surface in the Southern Ocean, which we identify as the major global pathway for old, pre-
524 industrial carbon to return to the surface and as the key source of Southern Ocean outgassing. The
525 importance of this isopycnal and pathway for supply of old, nutrient-rich IPDW to the surface of
526 the Southern Ocean was previously identified through the location of the IPDW oxygen minimum
527 (Talley, 2013). Here we highlight its relevance of being the major return pathway of CO_2 from the
528 deep ocean to the atmosphere. This pathway draws from a high-ΔPCO_2 pool in the mid-depth
529 northern Indo-Pacific basins, which exceeds current atmospheric CO_2 levels (400 µatm) by more
530 than 800 µatm and is the result of a slow accumulation of carbon due to the remineralization of
531 organic matter. The resulting high-PCO_2 IPDW propagates southward, where it subsequently
532 upwells in the high-latitude Southern Ocean, retaining a high-ΔPCO_2 signal that exceeds current
533 atmospheric levels by 175 µatm. Our findings thus provide observational evidence that there is a
534 substantial transport of old, pre-industrial CO_2 from the deep ocean to the atmosphere through the
535 Southern Ocean surface under present-day conditions. Therefore, interior ocean measurements
536 support the recent argument for a large natural CO_2 release at the surface in the open waters around
537 Antarctica (Bushinsky et al., 2019; Gray et al., 2018), sourced from relatively high PCO_2 water
538 that has upwelled to just beneath the mixed layer; this outgassing signal is best observed in winter
539 when deep mixing entrains the high-ΔPCO_2 IPDW to the surface (Prend et al., submitted).

We find that the vertical subsurface ΔPCO_2 gradient, and in particular the isopycnal that best characterizes its subsurface maximum, directly controls the meridional pattern of the Southern Ocean surface CO_2 fluxes. The maximum outgassing between the Subantarctic Front and the winter-time sea-ice edge is caused by a circumpolar band of high-ΔPCO_2 IPDW just beneath the surface mixed layers. This characteristic ring pattern of Southern Ocean outgassing and high subsurface ΔPCO_2 is due to the southward-rising isopycnal surfaces that project the vertical ΔPCO_2 maximum in IPDW onto the horizontal plane. The ring is circumpolar because the deep waters spiral southeastward with the ACC while they are rising, and are thus found all around Antarctica even though the original sources are localized boundary outflows from the Indian and Pacific basins (Tamsitt et al., 2017). Denser waters, such as NADW, reach the surface south of the maximum outgassing region in the ACC, and do not considerably contribute to the outgassing due to their lower ΔPCO_2. Thus, the vertical ΔPCO_2 distribution at mid-latitudes directly explains the characteristic ring structure of Southern Ocean CO_2 release (Figure 2a,e).

Deep ocean carbon content (DIC) is often used as a measure for Southern Ocean CO_2 release. However, we here have shown that only considering upwelling DIC can lead to misinterpretations, since the subsurface DIC structure critically differs from the subsurface ΔPCO_2 structure that controls the surface CO_2 fluxes. The DIC maximum occurs much deeper in the water column and remains high all the way to the bottom of the ocean, whereas ΔPCO_2 peaks shallower and declines with depth. In our analysis, we show that the vertical distribution of ΔPCO_2 and dissolved oxygen in the deep ocean are controlled primarily by the soft-tissue pump, whereas the vertical distribution of DIC is influenced by both the soft-tissue and the carbonate pumps, offsetting its maximum to deeper layers. This elevated carbon content (DIC) in the denser and deeper water masses, such as LCDW and AABW, is buffered by their carbon chemistry (high alkalinity) and colder temperatures, which prevents CO_2 outgassing from these waters. This reduced outgassing potential from higher alkalinity in the deeper waters is the result of a deeper depth of calcium carbonate dissolution compared to organic matter remineralization in the global ocean, which has been identified as a key mechanism for actively retaining carbon at depth over long time scales (Broecker & Peng, 1987; Hain et al., 2010; Krumhardt et al., 2020; Kwon et al., 2011; Toggweiler, 1999). Consequently, next to an adequate ocean circulation, a realistic representation of the vertical remineralization and dissolution profiles in the global ocean is an important pre-requisit for Earth

System Models to accurately simulate Southern Ocean CO_2 fluxes and the global ocean carbon cycle, as well as their response to climatic changes.

Model simulations project an enhanced future upwelling of deep waters in the Southern Ocean (Downes & Hogg, 2013) due to a poleward intensification of westerly winds (Bracegirdle et al., 2020) and changes in the surface buoyancy forcing (Bishop et al., 2016; Downes et al., 2018). Such an increased upwelling could substantially amplify the leakage of pre-industrial CO_2 from the deep ocean (Lovenduski et al., 2007; Toggweiler & Russell, 2008) and lead to a "saturation" of the anthropogenic CO_2 uptake by the ocean (Lovenduski et al., 2007; Le Quéré et al., 2007). However, there is still limited confidence in future projections of upwelling in the Southern Ocean (Meredith et al., 2019) since these models do not resolve mesoscale eddies (Bishop et al., 2016; Meredith et al., 2012; Morrison & Hogg, 2013) that are important for the ocean's carbon transport (Abernathey & Ferreira, 2015; Dufour et al., 2015) and suffer from large biases in their water mass structure (Beadling et al., 2020; Downes et al., 2018). In addition, global climate models struggle to produce the correct patterns and magnitudes (Lenton et al., 2013; Mongwe et al., 2018) and temporal variability (Gruber et al., 2019) of surface CO_2 fluxes in the Southern Ocean. Observational evidence derived from chlorofluorocarbon measurements points towards an increased upwelling since the early 1990s (Ting & Holzer, 2017; Waugh et al., 2013). However, recent findings also show that the relation between upwelling deep waters and changes in the surface CO_2 fluxes is much more complex and exhibits strong fluctuations on decadal time scales (DeVries et al., 2019; Landschützer et al., 2015). Our results imply that not only the strength of circulation changes in the Southern Ocean plays an important role in altering the release of CO_2 from the deep ocean to the atmosphere, but also the depth level from which waters are upwelled. Moreover, they also imply that changes in subsurface carbon chemistry could impact the deep ocean CO_2 release. These implications of our results highlight the importance of improving the subsurface carbon chemistry, water-mass structure, and circulation in global climate models in order to better assess future changes in atmospheric CO_2 in response to ocean circulation changes.

Acknowledgments

All data and tools underlying this analysis are openly available: Mapped GLODAP version 2 (https://www.glodap.info/index.php/mapped-data-product; https://doi.org/10.5194/essd-8-325-2016); SOCCOM float data (Snapshot 2021-05-05; https://doi.org/10.6075/J0T43SZG); globally

mapped CO_2 flux estimate based on the Surface Ocean CO_2 Atlas Database (SOCAT) and Southern Ocean Carbon and Climate Observations and Modeling (SOCCOM) biogeochemistry floats (1982 to 2017, NCEI Accession 0191304, Version 2.2; https://doi.org/10.25921/9hsn-xq82); Global monthly gridded sea surface pCO_2 product from 1982 onward and its monthly climatology (NCEI Accession 0160558, Version 5.5; https://doi.org/10.7289/V5Z899N6); CDIAC CO_2 flux estimated from air-sea difference in CO_2 partial pressure (revised October 2009; https://www.ldeo.columbia.edu/res/pi/CO2/carbondioxide/pages/air_sea_flux_2010.html); MATLAB Program Developed for CO_2 System Calculations (https://doi.org/10.3334/CDIAC/otg.CO2SYS_MATLAB_v1.1); NOAA/NSIDC Climate Data Record of Passive Microwave Sea Ice Concentration (Version 3, 1979-2018; https://doi.org/10.7265/N59P2ZTG).

This work was sponsored by NSF's Southern Ocean Carbon and Climate Observations and Modeling (SOCCOM, PLR-1425989) Project under the NSF Award PLR-1425989, supplemented by NASA (NNX14AP49G), and by the International Argo Program and the NOAA programs that contribute to it. H.C. was supported by SOCCOM. F.A.H. was supported by the SNSF grant numbers P2EZP2_175162 and P400P2_186681. K.S.J. thanks support from the David and Lucile Packard Foundation through the Monterey Bay Aquarium Research Institute. We are deeply thankful to Robert Key, Siv Lauvset, Are Olsen, and the large number of scientists, technicians, and funding agencies responsible for the collection and quality control of the high-quality ship-based data in GLODAPv2 (https://www.glodap.info/index.php/group) and for providing a gridded data product that underpins much of this work. We thank Joan Llort, Daniel Sigman, and Robert Toggweiler for comments and discussion on an earlier version of this paper.

Author contributions: H.C., F.A.H., and J.L.S. designed the study. H. C. and F.A.H conducted the analysis. F.A.H. and H.C. wrote the paper supported by J.L.S.. All authors discussed the results and contributed ideas.

References

Abernathey, R., & Ferreira, D. (2015). Southern Ocean isopycnal mixing and ventilation changes driven by winds. *Geophysical Research Letters*, *42*(23), 10357–10365. https://doi.org/10.1002/2015GL066238

Aldama-Campino, A., Fransner, F., Ödalen, M., Groeskamp, S., Yool, A., Döös, K., & Nycander, J. (2020). Meridional Ocean Carbon Transport. *Global Biogeochemical Cycles*, *34*(9),

e2019GB006336. https://doi.org/10.1029/2019GB006336

Anderson, L. A., & Sarmiento, J. L. (1994). Redfield ratios of remineralization determined by nutrient data analysis. *Global Biogeochemical Cycles*, *8*(1), 65–80. https://doi.org/10.1029/93GB03318

Arteaga, L., Haëntjens, N., Boss, E., Johnson, K. S., & Sarmiento, J. L. (2018). Assessment of Export Efficiency Equations in the Southern Ocean Applied to Satellite-Based Net Primary Production. *Journal of Geophysical Research: Oceans*, *123*(4), 2945–2964. https://doi.org/10.1002/2018JC013787

Beadling, R. L., Russell, J. L., Stouffer, R. J., Mazloff, M., Talley, L. D., Goodman, P. J., et al. (2020). Representation of Southern Ocean properties across Coupled Model Intercomparison Project generations: CMIP3 to CMIP6. *Journal of Climate*, *33*(15), 6555–6581. https://doi.org/10.1175/jcli-d-19-0970.1

Bishop, S. P., Gent, P. R., Bryan, F. O., Thompson, A. F., Long, M. C., Abernathey, R., et al. (2016). Southern Ocean Overturning Compensation in an Eddy-Resolving Climate Simulation. *Journal of Physical Oceanography*, *46*(5), 1575–1592. https://doi.org/10.1175/JPO-D-15-0177.1

Bracegirdle, T. J., Krinner, G., Tonelli, M., Haumann, F. A., Naughten, K. A., Rackow, T., et al. (2020). Twenty first century changes in Antarctic and Southern Ocean surface climate in CMIP6. *Atmospheric Science Letters*. https://doi.org/10.1002/asl.984

Broecker, W. S., & Peng, T.-H. (1987). The Role of CaCO3 Compenstation in the Glacial to Interglacial Atmospheric CO2 Change. *Global Biogeochemical Cycles*, *1*(1), 15–29. Retrieved from http://dx.doi.org/10.1029/GB001i001p00015

Broecker, W. S., & Peng, T. H. (1982). *Tracers in the sea*. *Eldigio Press*. https://doi.org/10.1016/0016-7037(83)90075-3

Broecker, W. S., & Peng, T. H. (1992). Interhemispheric transport of carbon dioxide by ocean circulation. *Nature*, *356*(6370), 587–589. https://doi.org/10.1038/356587a0

Bushinsky, S. M., Landschützer, P., Rödenbeck, C., Gray, A. R., Baker, D., Mazloff, M. R., et al. (2019). Reassessing Southern Ocean Air-Sea CO2 Flux Estimates With the Addition of Biogeochemical Float Observations. *Global Biogeochemical Cycles*, *33*(11), 1370–1388. https://doi.org/10.1029/2019GB006176

Carter, B. R., Feely, R. A., Williams, N. L., Dickson, A. G., Fong, M. B., & Takeshita, Y. (2018). Updated methods for global locally interpolated estimation of alkalinity, pH, and nitrate. *Limnology and Oceanography: Methods*, *16*(2), 119–131. https://doi.org/10.1002/lom3.10232

Chen, G. T., & Millero, F. J. (1979). Gradual increase of oceanic CO2. *Nature*, *277*(5693), 205–206. https://doi.org/10.1038/277205a0

DeVries, T., & Primeau, F. (2011). Dynamically and Observationally Constrained Estimates of Water-Mass Distributions and Ages in the Global Ocean. *Journal of Physical Oceanography*, *41*(12), 2381–2401. https://doi.org/10.1175/JPO-D-10-05011.1

DeVries, T., Le Quéré, C., Andrews, O., Berthet, S., Hauck, J., Ilyina, T., et al. (2019). Decadal

trends in the ocean carbon sink. *Proceedings of the National Academy of Sciences*, *116*(24), 201900371. https://doi.org/10.1073/pnas.1900371116

Dickson, A. G. (1990). Standard potential of the reaction : AgCl (s) + 1/2H2(g) = Ag (s) + HCl (aq), and the standard acidity constant of the ion HSO4- in synthetic sea water from 273 . 15 to 318 . 15 K. *The Journal of Chemical Thermodynamics*, *22*(3), 113–127.

Downes, S. M., & Hogg, A. M. (2013). Southern Ocean Circulation and Eddy Compensation in CMIP5 Models. *Journal of Climate*, *26*(18), 7198–7220. https://doi.org/10.1175/JCLI-D-12-00504.1

Downes, S. M., Spence, P., & Hogg, A. M. (2018). Understanding variability of the Southern Ocean overturning circulation in CORE-II models. *Ocean Modelling*, *123*, 98–109. https://doi.org/10.1016/j.ocemod.2018.01.005

Dufour, C. O., Griffies, S. M., de Souza, G. F., Frenger, I., Morrison, A. K., Palter, J. B., et al. (2015). Role of Mesoscale Eddies in Cross-Frontal Transport of Heat and Biogeochemical Tracers in the Southern Ocean. *Journal of Physical Oceanography*, *45*(12), 3057–3081. https://doi.org/10.1175/JPO-D-14-0240.1

Gent, P. R., & McWilliams, J. C. (1990). Isopycnal Mixing in Ocean Circulation Models. *Journal of Physical Oceanography*, *20*(1), 150–155. https://doi.org/10.1175/1520-0485(1990)020<0150:IMIOCM>2.0.CO;2

Gray, A. R., Johnson, K. S., Bushinsky, S. M., Riser, S. C., Russell, J. L., Talley, L. D., et al. (2018). Autonomous Biogeochemical Floats Detect Significant Carbon Dioxide Outgassing in the High-Latitude Southern Ocean. *Geophysical Research Letters*, *45*(17), 9049–9057. https://doi.org/10.1029/2018GL078013

Gruber, N., & Sarmiento, J. L. (2002). *Large scale biochemical/physical interactions in elemental cycles. The Sea: biological-physical interactions in the oceans* (Vol. 12).

Gruber, N., Gloor, M., Mikaloff Fletcher, S. E., Doney, S. C., Dutkiewicz, S., Follows, M. J., et al. (2009). Oceanic sources, sinks, and transport of atmospheric CO2. *Global Biogeochemical Cycles*, *23*(1), GB1005. https://doi.org/10.1029/2008GB003349

Gruber, N., Landschützer, P., & Lovenduski, N. S. (2019). The Variable Southern Ocean Carbon Sink. *Annual Review of Marine Science*, *11*(1), 159–186. https://doi.org/10.1146/annurev-marine-121916-063407

Hain, M. P., Sigman, D. M., & Haug, G. H. (2010). Carbon dioxide effects of Antarctic stratification, North Atlantic Intermediate Water formation, and subantarctic nutrient drawdown during the last ice age: Diagnosis and synthesis in a geochemical box model. *Global Biogeochemical Cycles*, *24*(4), GB4023--. https://doi.org/10.1029/2010GB003790

Haumann, F. A., Gruber, N., Münnich, M., Frenger, I., & Kern, S. (2016). Sea-ice transport driving Southern Ocean salinity and its recent trends. *Nature*, *537*(7618), 89–92. https://doi.org/10.1038/nature19101

van Heuven, S., Pierrot, D., Rae, J. W. B., Lewis, E., & Wallace, D. W. R. (2011). MATLAB Program Developed for CO2 System Calculations. *ORNL/CDIAC-105b. Carbon Dioxide Information Analysis Center, Oak Ridge National Laboratory, U.S. Department of Energy, Oak Ridge, Tennessee*. https://doi.org/10.3334/CDIAC/otg.CO2SYS_MATLAB_v1.1

Holzer, M., DeVries, T., & Lavergne, C. de. (2021). Diffusion controls the ventilation of a Pacific Shadow Zone above abyssal overturning. *Nature Communications*, *12*(1), 1–13. https://doi.org/10.1038/s41467-021-24648-x

Iudicone, D., Rodgers, K. B., Stendardo, I., Aumont, O., Madec, G., Bopp, L., et al. (2011). Water masses as a unifying framework for understanding the Southern Ocean Carbon Cycle. *Biogeosciences*, *8*(5), 1031–1052. https://doi.org/10.5194/bg-8-1031-2011

Jackett, D. R., & McDougall, T. J. (1997). A Neutral Density Variable for the World's Oceans. *Journal of Physical Oceanography*, *27*(2), 237–263. https://doi.org/10.1175/1520-0485(1997)027<0237:ANDVFT>2.0.CO;2

Jiang, L., Feely, R. A., Carter, B. R., Greeley, D. J., Gledhill, D. K., & Arzayus, K. M. (2015). Global Biogeochemical Cycles saturation state in the global oceans. *Global Biogeochemical Cycles*, *29*(10), 1656–1673. https://doi.org/10.1002/2015GB005198.Received

Johnson, K. S., Jannasch, H. W., Coletti, L. J., Elrod, V. A., Martz, T. R., Takeshita, Y., et al. (2016). Deep-Sea DuraFET: A Pressure Tolerant pH Sensor Designed for Global Sensor Networks. *Analytical Chemistry*, *88*(6), 3249–3256. https://doi.org/10.1021/acs.analchem.5b04653

Johnson, K. S., Plant, J. N., Coletti, L. J., Jannasch, H. W., Sakamoto, C. M., Riser, S. C., et al. (2017). Biogeochemical sensor performance in the SOCCOM profiling float array. *Journal of Geophysical Research: Oceans*. https://doi.org/10.1002/2017JC012838

Johnson, K. S., Riser, S. C., Boss, E. S., Talley, L. D., Sarmiento, J. L., Swift, D. D., et al. (2021). SOCCOM float data - Snapshot 2021-05-05. In *Southern Ocean Carbon and Climate Observations and Modeling (SOCCOM) Float Data Archive*. UC San Diego Library Digital Collections. https://doi.org/10.6075/J0T43SZG

Key, R. M., Kozyr, A., Sabine, C. L., Lee, K., Wanninkhof, R., Bullister, J. L., et al. (2004). A global ocean carbon climatology: Results from Global Data Analysis Project (GLODAP). *Global Biogeochemical Cycles*, *18*(4), GB4031. https://doi.org/10.1029/2004GB002247

Key, R. M., Olsen, A., Heuven, S. van, Lauvset, S. K., Velo, A., Lin, X., et al. (2015). Global Ocean Data Analysis Project, Version 2 (GLODAPv2), ORNL/CDIAC-162, ND-P093. Oak Ridge, Tennessee: Carbon Dioxide Information Analysis Center, Oak Ridge National Laboratory, US Department of Energy. https://doi.org/10.3334/CDIAC/OTG.NDP093_GLODAPv2

Krumhardt, K. M., Long, M. C., Lindsay, K., & Levy, M. N. (2020). Southern Ocean Calcification Controls the Global Distribution of Alkalinity. *Global Biogeochemical Cycles*, *34*(12), e2020GB006727. https://doi.org/10.1029/2020GB006727

Kwon, E. Y., Primeau, F., & Sarmiento, J. L. (2009). The impact of remineralization depth on the air-sea carbon balance. *Nature Geoscience*, *2*(9), 630–635. https://doi.org/10.1038/ngeo612

Kwon, E. Y., Sarmiento, J. L., Toggweiler, J. R., & DeVries, T. (2011). The control of atmospheric pCO2 by ocean ventilation change: The effect of the oceanic storage of biogenic carbon. *Global Biogeochemical Cycles*, *25*(3), GB3026. https://doi.org/10.1029/2011GB004059

Landschützer, P., Gruber, N., Haumann, F. A., Rödenbeck, C., Bakker, D. C. E., Heuven, S. Van, et al. (2015). The reinvigoration of the Southern Ocean carbon sink. *Science*, *349*, 1221–1224.

https://doi.org/10.1126/science.aab2620

Landschützer, P., Gruber, N., & Bakker, D. C. E. (2016). Decadal variations and trends of the global ocean carbon sink. *Global Biogeochemical Cycles*, *30*(10), 1396–1417. https://doi.org/10.1002/2015GB005359

Landschützer, P., Bushinsky, S., & Gray, A. R. (2019). A combined globally mapped CO2 flux estimate based on the Surface Ocean CO2 Atlas Database (SOCAT) and Southern Ocean Carbon and Climate Observations and Modeling (SOCCOM) biogeochemistry floats from 1982 to 2017 (NCEI Accession 0191304). Version 2.2. NOAA National Centers for Environmental Information. https://doi.org/10.25921/9hsn-xq82

Landschützer, P., Gruber, N., & Bakker, D. C. E. (2020). An observation-based global monthly gridded sea surface pCO2 product from 1982 onward and its monthly climatology (NCEI Accession 0160558). Version 5.5. NOAA National Centers for Environmental Information. https://doi.org/10.7289/V5Z899N6

Lauvset, S. K., Key, R. M., Olsen, A., Van Heuven, S., Velo, A., Lin, X., et al. (2016). A new global interior ocean mapped climatology: The 1° × 1° GLODAP version 2. *Earth System Science Data*, *8*(2), 325–340. https://doi.org/10.5194/essd-8-325-2016

Lee, K., Kim, T. W., Byrne, R. H., Millero, F. J., Feely, R. A., & Liu, Y. M. (2010). The universal ratio of boron to chlorinity for the North Pacific and North Atlantic oceans. *Geochimica et Cosmochimica Acta*, *74*(6), 1801–1811. https://doi.org/10.1016/j.gca.2009.12.027

Lenton, A., Tilbrook, B., Law, R. M., Bakker, D., Doney, S. C., Gruber, N., et al. (2013). Sea–air CO_2 fluxes in the Southern Ocean for the period 1990–2009. *Biogeosciences*, *10*(6), 4037–4054. https://doi.org/10.5194/bg-10-4037-2013

Lovenduski, N. S., Gruber, N., Doney, S. C., & Lima, I. D. (2007). Enhanced CO2 outgassing in the Southern Ocean from a positive phase of the Southern Annular Mode. *Global Biogeochemical Cycles*, *21*(2), GB2026. https://doi.org/10.1029/2006GB002900

Lueker, T. J., Dickson, A. G., & Keeling, C. D. (2000). Ocean pCO2 calculated from dissolved inorganic carbon, alkalinity, and equations for K1 and K2: Validation based on laboratory measurements of CO2 in gas and seawater at equilibrium. *Marine Chemistry*, *70*(1–3), 105–119. https://doi.org/10.1016/S0304-4203(00)00022-0

MacGilchrist, G. A., Naveira Garabato, A. C., Brown, P. J., Jullion, L., Bacon, S., Bakker, D. C. E., et al. (2019). Reframing the carbon cycle of the subpolar Southern Ocean. *Science Advances*, *5*(8), eaav6410. https://doi.org/10.1126/sciadv.aav6410

Martin, J. H., Knauer, G. A., Karl, D. M., & Broenkow, W. W. (1987). VERTEX: carbon cycling in the northeast Pacific. *Deep Sea Research Part A, Oceanographic Research Papers*, *34*(2), 267–285. https://doi.org/10.1016/0198-0149(87)90086-0

Meier, W. N., Fetterer, F., Savoie, M., Mallory, S., Duerr, R., & Stroeve, J. (2017). NOAA/NSIDC Climate Data Record of Passive Microwave Sea Ice Concentration, Version 3, 1979-2018. Boulder, Colorado USA: NSIDC: National Snow and Ice Data Center. https://doi.org/10.7265/N59P2ZTG

Meredith, M., Sommerkorn, M., Cassotta, S., Derksen, C., Ekaykin, A., Hollowed, A., et al. (2019). Polar Regions. In H.-O. Pörtner, D. C. Roberts, V. Masson-Delmotte, P. Zhai, M.

Tignor, E. Poloczanska, et al. (Eds.), *IPCC Special Report on the Ocean and Cryosphere in a Changing Climate*.

Meredith, M. P., Naveira Garabato, A. C., Hogg, A. M., & Farneti, R. (2012). Sensitivity of the overturning circulation in the Southern Ocean to decadal changes in wind forcing. *Journal of Climate*, *25*(1), 99–110. https://doi.org/10.1175/2011JCLI4204.1

Mikaloff Fletcher, S. E., Gruber, N., Jacobson, A. R., Gloor, M., Doney, S. C., Dutkiewicz, S., et al. (2007). Inverse estimates of the oceanic sources and sinks of natural CO2 and the implied oceanic carbon transport. *Global Biogeochemical Cycles*, *21*(1), GB1010. https://doi.org/10.1029/2006GB002751

Mongwe, N. P., Vichi, M., & Monteiro, P. M. S. (2018). The seasonal cycle of CO2 and CO2 fluxes in the Southern Ocean: diagnosing anomalies in CMIP5 Earth system models. *Biogeosciences*, *15*(9), 2851–2872. https://doi.org/10.5194/bg-15-2851-2018

Morrison, A. K., & Hogg, A. M. (2013). On the Relationship between Southern Ocean Overturning and ACC Transport. *Journal of Physical Oceanography*, *43*(1), 140–148. https://doi.org/10.1175/JPO-D-12-057.1

Morrison, A. K., Frölicher, T. L., & Sarmiento, J. L. (2015). Upwelling in the Southern Ocean. *Physics Today*, *68*(1), 27–32. https://doi.org/10.1063/PT.3.2654

Olsen, A., Key, R. M., van Heuven, S., Lauvset, S. K., Velo, A., Lin, X., et al. (2016). The Global Ocean Data Analysis Project version 2 (GLODAPv2) – an internally consistent data product for the world ocean. *Earth System Science Data*, *8*(2), 297–323. https://doi.org/10.5194/essd-8-297-2016

Orsi, A. H., Whitworth, T., & Nowlin, W. D. (1995). On the meridional extent and fronts of the Antarctic Circumpolar Current. *Deep-Sea Research Part I*, *42*(5), 641–673. https://doi.org/10.1016/0967-0637(95)00021-W

Orsi, A. H., Johnson, G. C., & Bullister, J. L. (1999). Circulation, mixing, and production of Antarctic Bottom Water. *Progress in Oceanography*, *43*(1), 55–109. https://doi.org/10.1016/S0079-6611(99)00004-X

Peng, G., Meier, W. N., Scott, D. J., & Savoie, M. H. (2013). A long-term and reproducible passive microwave sea ice concentration data record for climate studies and monitoring. *Earth System Science Data*, *5*(2), 311–318. https://doi.org/10.5194/essd-5-311-2013

Perez, F. F., & Fraga, F. (1987). Association constant of fluoride and hydrogen ions in seawater. *Marine Chemistry*, *21*(2), 161–168. https://doi.org/10.1016/0304-4203(87)90036-3

Prend, C. J., Gray, A. R., Talley, L. D., Gille, S. T., Haumann, F. A., Johnson, K. S., et al. (n.d.). Indo-Pacific sector dominates Southern Ocean carbon outgassing. *Submitted to Nature Communications*.

Le Quéré, C., Rödenbeck, C., Buitenhuis, E. T., Conway, T. J., Langenfelds, R., Gomez, A., et al. (2007). Saturation of the Southern Ocean CO2 Sink due to recent climate change. *Science*, *316*(5832), 1735–1738. https://doi.org/10.1126/science.1136188

Sarmiento, J. L., & Gruber, N. (2006). *Ocean Biogeochemical Dynamics*. *Princeton University Press*. Princeton, NJ: Princeton University Press. Retrieved from

http://www.up.ethz.ch/publications/books.html

Sarmiento, J. L., Toggweiler, J. R., Najjar, R., Webb, D. J., Jenkins, W. J., Wunsch, C., et al. (1988). Ocean Carbon-Cycle Dynamics and Atmospheric pCO2. *Philosophical Transactions of the Royal Society A*, *325*(1583), 3–21. https://doi.org/10.1098/rsta.1988.0039

Skinner, L. C., Fallon, S., Waelbroeck, C., Michel, E., & Barker, S. (2010). Ventilation of the deep Southern Ocean and deglacial CO2 rise. *Science*, *328*(May), 1147–1152. https://doi.org/10.1126/science.1183627

Speer, K., Rintoul, S. R., & Sloyan, B. (2000). The Diabatic Deacon Cell. *Journal of Physical Oceanography*, *30*(12), 3212–3222. https://doi.org/10.1175/1520-0485(2000)030<3212:TDDC>2.0.CO;2

Takahashi, T., Sutherland, S. C., Sweeney, C., Poisson, A., Metzl, N., Tilbrook, B., et al. (2002). Global sea-air CO2 flux based on climatological surface ocean pCO2, and seasonal biological and temperature effects. *Deep Sea Research Part II: Topical Studies in Oceanography*, *49*(9), 1601–1622. https://doi.org/10.1016/S0967-0645(02)00003-6

Takahashi, T., Sutherland, S. C., Wanninkhof, R., Sweeney, C., Feely, R. A., Chipman, D. W., et al. (2009). Climatological mean and decadal change in surface ocean pCO2 , and net sea-air CO2 flux over the global oceans. *Deep-Sea Research Part II: Topical Studies in Oceanography*, *56*(8–10), 554–577. https://doi.org/10.1016/j.dsr2.2008.12.009

Talley, L. D. (2013). Closure of the global overturning circulation through the Indian, Pacific, and Southern Oceans: Schematics and transports. *Oceanography*, *26*(1), 80–97. https://doi.org/10.5670/oceanog.2013.07

Tamsitt, V., Drake, H. F., Morrison, A. K., Talley, L. D., Dufour, C. O., Gray, A. R., et al. (2017). Spiraling pathways of global deep waters to the surface of the Southern Ocean. *Nature Communications*, *8*(1), 1–10. https://doi.org/10.1038/s41467-017-00197-0

Tamsitt, V., Talley, L. D., & Mazloff, M. R. (2019). A Deep Eastern Boundary Current Carrying Indian Deep Water South of Australia. *Journal of Geophysical Research: Oceans*, *124*(3), 2218–2238. https://doi.org/10.1029/2018JC014569

Ting, Y. H., & Holzer, M. (2017). Decadal changes in Southern Ocean ventilation inferred from deconvolutions of repeat hydrographies. *Geophysical Research Letters*, *44*(11), 5655–5664. https://doi.org/10.1002/2017GL073788

Toggweiler, J. R. (1999). Variation of atmospheric CO2 by ventilation of the ocean's deepest water. *Paleoceanography*, *14*(5), 571. https://doi.org/10.1029/1999PA900033

Toggweiler, J. R., & Russell, J. (2008). Ocean circulation in a warming climate. *Nature*, *451*(7176), 286–288. https://doi.org/10.1038/nature06590

Toggweiler, J. R., & Samuels, B. (1995). Effect of drake passage on the global thermohaline circulation. *Deep Sea Research Part I: Oceanographic Research Papers*, *42*(4), 477–500. https://doi.org/10.1016/0967-0637(95)00012-U

Volk, T., & Hoffert, M. I. (1985). Ocean Carbon Pumps: Analysis of Relative Strengths and Efficiencies in Ocean-Driven Atmospheric CO2 Changes. In E. Sundquist & W. Broecker (Eds.), *The Carbon Cycle and Atmospheric CO2: Natural Variations Archean to Present*

(Vol. 32, pp. 99–110). American Geophysical Union (AGU). https://doi.org/10.1029/GM032P0099

Waugh, D. W., Primeau, F., DeVries, T., & Holzer, M. (2013). Recent changes in the ventilation of the southern oceans. *Science*, *339*(6119), 568–570. https://doi.org/10.1126/science.1225411

Williams, N. L., Juranek, L. W., Feely, R. A., Johnson, K. S., Sarmiento, J. L., Talley, L. D., et al. (2017). Calculating surface ocean pCO2 from biogeochemical Argo floats equipped with pH: An uncertainty analysis. *Global Biogeochemical Cycles*, *31*(3), 591–604. https://doi.org/10.1002/2016GB005541

Wilson, E. A., Riser, S. C., Campbell, E. C., Wong, A. P. S., Wilson, E. A., Riser, S. C., et al. (2019). Winter Upper-Ocean Stability and Ice–Ocean Feedbacks in the Sea Ice–Covered Southern Ocean. *Journal of Physical Oceanography*, *49*(4), 1099–1117. https://doi.org/10.1175/JPO-D-18-0184.1

Wu, Y., Hain, M. P., Humphreys, M. P., Hartman, S., & Tyrrell, T. (2019). What drives the latitudinal gradient in open-ocean surface dissolved inorganic carbon concentration? *Biogeosciences*, *16*(13), 2661–2681. https://doi.org/10.5194/bg-16-2661-2019